UC Irvine

UC Irvine Previously Published Works

Title

Segmentation of the Prostate Transition Zone and Peripheral Zone on MR Images with Deep Learning

Permalink

https://escholarship.org/uc/item/6k1853wf

Journal

Radiology Imaging Cancer, 3(3)

ISSN

2638-616X

Authors

Bardis, Michelle
Houshyar, Roozbeh
Chantaduly, Chanon
et al.

Publication Date

2021-05-01

DOI

10.1148/rycan.2021200024

Peer reviewed

eScholarship.org Powered by the California Digital Library
University of California

Radiology: Imaging Cancer

ORIGINAL RESEARCH

Segmentation of the Prostate Transition Zone and Peripheral Zone on MR Images with Deep Learning

Michelle Bardis, MS • Roozbeh Houshyar, MD • Chanon Chantaduly, BS • Karen Tran-Harding, MD • Alexander Ushinsky, MD • Chantal Chahine, MD • Mark Rupasinghe, BS • Daniel Chow, MD • Peter Chang, MD

From the Department of Radiological Sciences, University of California, Irvine, 101 The City Drive South, Building 55, Suite 201, Orange, CA 92868 (M.B., R.H., K.T.H., C. Chahine, M.R.); Center for Artificial Intelligence in Diagnostic Medicine, University of California, Irvine, Irvine, Calif (C. Chantaduly, D.C., P.C.); and Mallinckrodt Institute of Radiology, Washington University School of Medicine, St Louis, Mo (A.U.). Received March 23, 2020; revision requested April 8; revision received February 3, 2021; accepted February 25. **Address correspondence to** M.B. (e-mail: *mbardis@hs.uci.edu*).

Conflicts of interest are listed at the end of this article.

Radiology: Imaging Cancer 2021; 3(3):e200024 • https://doi.org/10.1148/rycan.2021200024 • Content codes: AI GU MR

Purpose: To develop a deep learning model to delineate the transition zone (TZ) and peripheral zone (PZ) of the prostate on MR images.

Materials and Methods: This retrospective study was composed of patients who underwent a multiparametric prostate MRI and an MRI/transrectal US fusion biopsy between January 2013 and May 2016. A board-certified abdominal radiologist manually segmented the prostate, TZ, and PZ on the entire data set. Included accessions were split into 60% training, 20% validation, and 20% test data sets for model development. Three convolutional neural networks with a U-Net architecture were trained for automatic recognition of the prostate organ, TZ, and PZ. Model performance for segmentation was assessed using Dice scores and Pearson correlation coefficients.

Results: A total of 242 patients were included (242 MR images; 6292 total images). Models for prostate organ segmentation, TZ segmentation, and PZ segmentation were trained and validated. Using the test data set, for prostate organ segmentation, the mean Dice score was 0.940 (interquartile range, 0.930–0.961), and the Pearson correlation coefficient for volume was 0.981 (95% CI: 0.966, 0.989). For TZ segmentation, the mean Dice score was 0.910 (interquartile range, 0.894–0.938), and the Pearson correlation coefficient for volume was 0.992 (95% CI: 0.985, 0.995). For PZ segmentation, the mean Dice score was 0.774 (interquartile range, 0.727–0.832), and the Pearson correlation coefficient for volume was 0.927 (95% CI: 0.870, 0.957).

Conclusion: Deep learning with an architecture composed of three U-Nets can accurately segment the prostate, TZ, and PZ.

Supplemental material is available for this article.

© RSNA, 2021

Prostate cancer is the second most common cancer in men, which resulted in 180 890 new cases and 26 120 deaths in 2016 (1,2). A key challenge that patients and clinicians face is the lack of noninvasive tools that differentiate aggressive prostate cancers from nonaggressive types (3). As a result, only one death is avoided for every 48 treated men (3). This overtreatment results in potentially unnecessary procedures, systemic therapy, and patient anxiety (4,5). Conversely, nearly 25% of men with normal prostate-specific antigen levels at prostate cancer screening are ultimately upgraded to a higher-grade cancer (6). As a result, the Prostate Imaging Reporting and Data System (PI-RADS) (7) was developed to improve prostate cancer characterization and prediction at multiparametric MRI. The PI-RADS system assigns a score between 1 and 5 to each prostate lesion. A lesion with a very low suspicion of malignancy receives a 1, while a lesion with very high suspicion of malignancy earns a 5 (8). However, the first branch point in the PI-RADS scoring system is the lesion's location in the transition zone (TZ) or peripheral zone (PZ) (8). If a lesion is located in the TZ, diffusion-weighted imaging contributes to the PI-RADS score. By contrast, if a lesion is in the PZ, dynamic contrast enhancement contributes to the PI-RADS score (9).

Although the localization of a lesion to a zone is crucial, segmentation of the TZ and PZ remains a challenge. TZ structure substantially changes due to benign prostatic hyperplasia, a normal process of aging, and becomes more difficult to segment (10). The PZ resembles the seminal vesicles at the superior portion of the prostate and can be harder to identify (11). The PZ border itself varies greatly per patient due to glandular enlargement and may be difficult to distinguish (11). Both TZ and PZ can also resemble blood vessels anterior to the prostate's midsection (11). Because TZ and PZ segmentations remain difficult, and their delineations are fundamental for assigning a PI-RADS score, a clinical tool is needed that could optimize recognizing their borders.

To fulfill this need for improved TZ and PZ identification, a deep learning algorithm could be used to segment these regions. Because a multiparametric MR image generally contains more than a million voxels (12), the systemic evaluation of MR images becomes an ideal challenge for deep learning algorithms. Deep learning algorithms have already been used with prostate MR images, and their ability to identify the prostate organ's borders has made substantial progress (13,14). The purpose of this study was to build upon these prior efforts by using a larger data set and

This copy is for personal use only. To order printed copies, contact reprints@rsna.org

Abbreviations

CNN = convolutional neural network, PI-RADS = Prostate Imaging Reporting and Data System, PZ = peripheral zone, TRUS = transrectal US, TZ = transition zone

Summary

The prostate transition zone and peripheral zone can be segmented accurately with deep learning algorithms.

Key Points

- Deep learning can be used to identify and segment prostate zones.
- Using the developed model, the mean Dice scores for segmentation were 0.940 for the whole prostate, 0.914 for transition zone, and 0.776 for peripheral zone.

Keywords

- MRI, Genital/Reproductive, Prostate, Neural Networks

two parallel neural networks that specialize in localization and classification for both TZ and PZ segmentation.

Materials and Methods

Institutional Review Board Approval

Approval was granted from the institutional review board for this retrospective, Health Insurance Portability and Accountability Act–compliant study. A portion of the data set used in this study was previously used for prostate identification and training size optimization with results published in two studies (15,16).

Patient Selection

A data set was composed of patients who met the following inclusion criteria: patients who underwent a multiparametric MRI with subsequent 12-core Artemis three-dimensional transrectal US (TRUS)–guided biopsy (Eigen) and patients who underwent an MRI/TRUS fusion biopsy using Artemis and ProFuse software (Eigen) between January 2013 and May 2016. The exclusion criteria were: *(a)* age younger than 40 years, *(b)* patients for whom complete follow-up data were not available, *(c)* and patients who underwent both MRI/TRUS fusion biopsy and random 12-core biopsy.

Image Acquisition

Prostate multiparametric MR images were obtained with two different scanners: a Philips Ingenia 3-T MRI scanner (Philips Healthcare) and a Siemens Magnetom Trio 3-T MRI scanner (Siemens Healthineers). The PI-RADS v2 protocol was followed during image acquisition. The following parameters were used for imaging: turbo spin-echo and echo-planar acquisition sequence; echo train length, 25; repetition time, 7300 msec; echo time, 108 msec; flip angle, 150°; field of view, 200 × 200 voxels; matrix size, 256 × 205; section thickness, 3 mm; section spacing, 3 mm; and using a body coil.

Ground Truth Segmentation

The prostate multiparametric MRI data were transferred from the picture archiving and communication system and de-identified before being transferred to an institutional review board–approved research MongoDB database (MongoDB). From the database, the prostate organ, TZ, and PZ segmentations were completed with an in-house proprietary image viewing and segmenting tool. Figure 1 shows examples of the TZ and PZ. Ten radiologists worked on prostate organ segmentations, and one radiologist completed the TZ and PZ segmentations (K.T.H.). A board-certified subspecialty-trained abdominal radiologist with more than 10 years of experience with multiparametric prostate MRI reviewed of all the segmentations and revised them as necessary (R.H.). This proprietary tool enabled the radiologist to complete any updates on the segmentations that could be easily integrated into neural network training and validation.

Overall Framework

This study's automated pipeline consisted of three convolutional neural networks (CNNs) (Fig 2). Each of these CNNs was implemented with a customized hybrid three-dimensional/two-dimensional (3D/2D) U-Net architecture. The networks were called U-Net$_A$, U-Net$_B$, and U-Net$_C$ (Fig 4). U-Net$_A$ was responsible for prostate gland localization by creating a bounding box around the prostate as detailed in Appendix E1 (supplement). This bounding box was then used as the input for both U-Net$_B$ and U-Net$_C$, which were run in parallel.

U-Net$_B$ completed gland localization by segmenting the entire prostate. This CNN produced an output that delineated the borders of the entire prostate. U-Net$_C$ performed classification by differentiating between the TZ and PZ. The portion of the data set which had the TZ and PZ regions segmented was used to train U-Net$_C$. U-Net$_C$ created an output that identified the border between the TZ and PZ. The outputs of U-Net$_B$ and U-Net$_C$ were then combined to create separate segmentations of the TZ and PZ. In the final output, the TZ was defined as the intersection between U-Net$_B$'s prostate output and U-Net$_C$'s TZ output. Similarly, the PZ was identified as the intersection between U-Net$_B$'s prostate output and U-Net$_C$'s PZ output.

Image Preprocessing

For U-Net$_A$, the prostate T2-weighted axial sections were all resized to a resolution of 256 × 256 and a section separation of 3 mm. For U-Net$_B$ and U-Net$_C$, the prostate T2-weighted axial sections were all set to a resolution of 128 × 128 and a section distance of 1 mm. After the images were resampled to the same resolution by each U-Net, normalization was performed by deriving the mean and standard deviation of image signal intensities during each database retrieval.

Implementation

The U-Net architecture was selected for all three CNNs because it performed both localization and classification on each pixel with limited training data (17). The U-Net's design consisted of two pathways that performed both downsampling and upsampling. Classification was completed on the downsampling pathway while localization was accomplished on the upsampling pathway with skip connections. The ar-

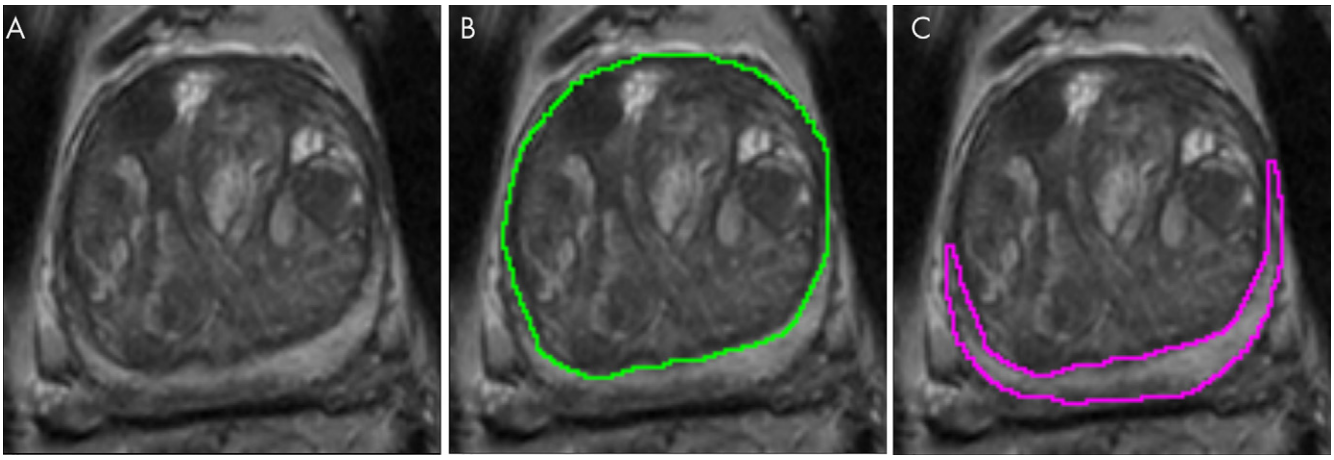

Figure 1: *A*, Axial T2-weighted section of a prostate with marked benign prostatic hyperplasia. *B*, The transition zone is shown in green, while, *C*, the peripheral zone is displayed in pink.

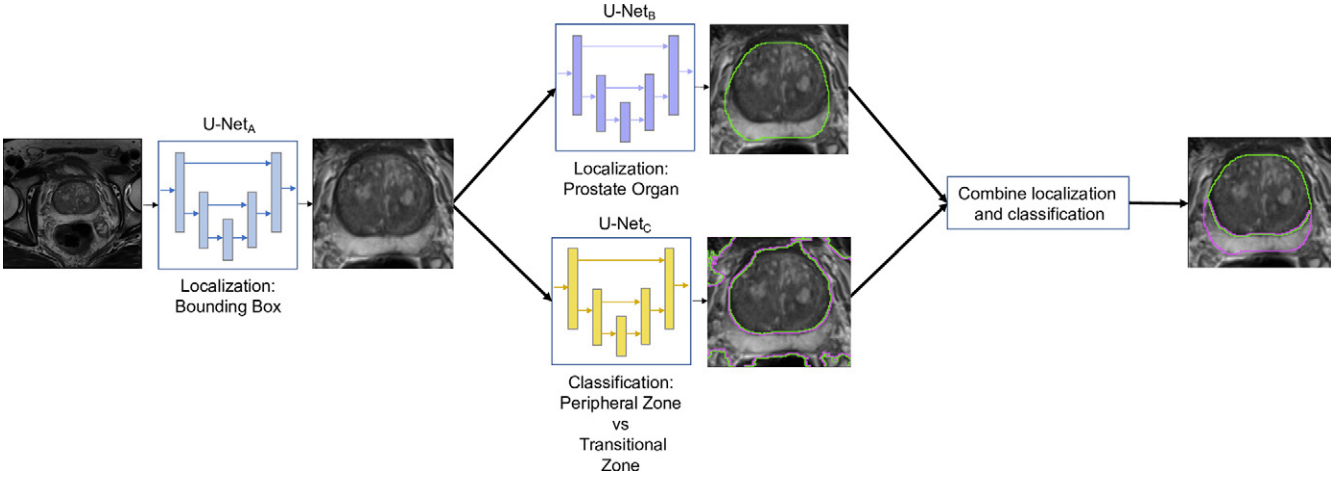

Figure 2: Three convolutional neural networks were combined to segment the transition zone (TZ) and the peripheral zone (PZ). The T2-weighted prostate MR image is first passed through U-Net$_A$, which performs localization and creates a bounding box around the prostate that narrows the field of view. This output is then passed simultaneously to U-Net$_B$ and U-Net$_C$. U-Net$_B$ completes further localization by segmenting out the prostate organ itself, while U-Net$_C$ classifies each pixel as either TZ or PZ. U-Net$_B$'s output is then used to identify the voxels in U-Net$_C$ that belong in the prostate. After the appropriate voxels are selected in U-Net$_C$'s output, the final output with TZ and PZ segmentations is shown.

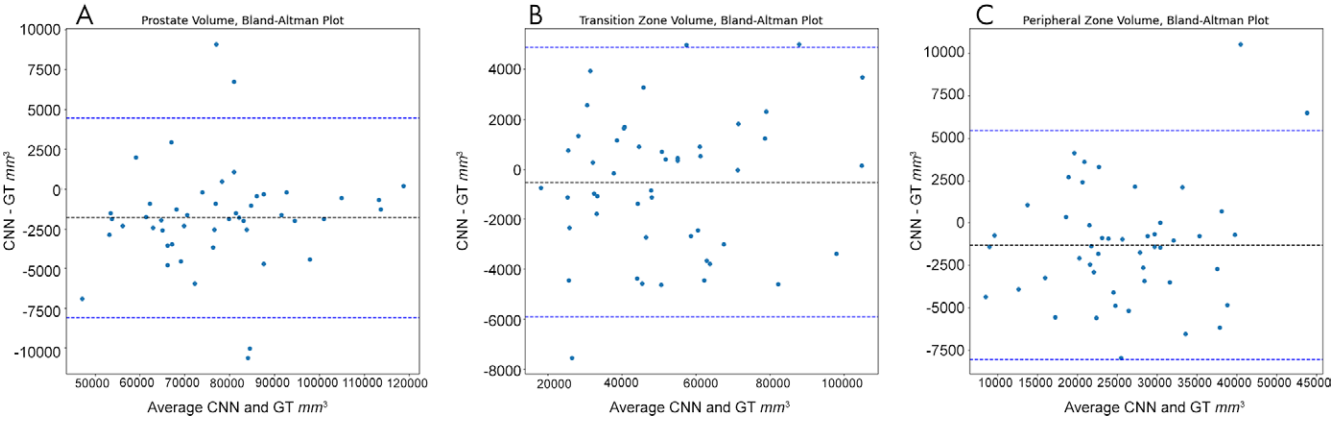

Figure 3: The reliability and accuracy of the neural networks to estimate volume of the prostate, transition zone, and peripheral zone are shown with Bland-Altman plots. *A–C*, The dashed black line represents the average difference. The dashed blue lines show 2 standard deviations of the difference above and below the average difference. CNN = convolutional neural network, GT = ground truth.

chitecture for all three U-Nets built upon the original U-Net design by extending its training from two dimensions to three dimensions and was labeled as a hybrid 3D/2D U-Net. Instead of training on a single axial section, all three U-Nets trained by examining voxels from five axial sections simultaneously. All three U-Nets also used the same structure for each layer: batch normalization, convolution, rectified linear unit activation, and either downsampling or upsampling. U-Net$_A$ downsampled the image until it collapsed into a 1 × 1 × 1 matrix before upsampling started; U-Net$_B$ and U-Net$_C$ downscaled the image to a 1 × 8 × 8 matrix before upsampling began. U-Net$_A$ used a batch size equal to 32 and a total of nine layers that contained between eight and 128 filters. Both U-Net$_B$ and U-Net$_C$ used a batch size equal to eight and a total of six layers that consisted of four to 64 filters.

The accessions were randomly partitioned into three categories: training (60%), validation (20%), or test (20%). The neural networks were fitted with training data, performance was assessed during training with validation data, and the results were calculated with test data. The hyperparameters were tuned when each neural network run was completed and the validation data were used to evaluate the model's performance. After the weights were established from training, the final results were established by then running inference with the test data that the model had not ever previously seen. A graphics processing unit–optimized workstation that uses 4 GeForce GTX 1080 Ti cards (11 GB, Pascal microarchitecture; NVIDIA) was used to train the U-Nets. The software was coded in Python 3.6 with the TensorFlow r2.10 library (Apache 2.0 license).

Network Details

The three U-Nets had their initial weights set by a heuristic defined by He et al (18) to avoid vanishing or exploding gradients. The Adam algorithm was then implemented for updating the weights based on training data. The Adam method had a straightforward implementation and was well matched for deep learning algorithms (19). The learning rate for Adam on all three CNNs was 1×10^{-3}, and the exponential decay rates for the moment estimates, b_1 and b_2, were set to 0.9 and 0.999, respectively. U-Net$_A$, U-Net$_B$, and U-Net$_C$ were trained for 50 000, 18 000, and 3800 iterations, respectively.

Statistical Analysis

This study was assessed with two metrics: Dice score (Sørensen-Dice coefficient) and Pearson correlation coefficient (*r*). The Dice score provides a metric that evaluates the algorithm's execution by comparing its segmented output to the ground truth. In this study, the Dice scores for the PZ, TZ, and whole prostate were calculated. The Dice score is defined with this formula:

$$\text{Dice} = \frac{2 \mid X \cap Y \mid}{\mid X \mid + \mid Y \mid} \quad (1).$$

The Dice score calculates the overlap between the ground truth and the neural network's inference. A Dice score of 0 indicates no intersection, and a Dice score of 1 represents perfect overlap. It is the most customary measure of neural network performance (20).

The Pearson correlation coefficient was used to reflect the algorithm's capability to calculate volume. The neural network's estimated volume was compared against the actual volume for the PZ, TZ, and whole prostate. The CI was calculated for the Dice score and Pearson correlation coefficient and reflects the precision of these metrics. For both the Dice score and Pearson correlation coefficient, the confidence level of 95% was calculated (21). The CI formula is:

$$CI = \bar{x} \pm z \frac{s}{\sqrt{n}} \quad (2),$$

where $\bar{x}$ is the sample mean, z is the 97.5th percentile of the standard normal distribution and equals 1.96 because the confidence level was 95%, s is the sample standard deviation, and n is the sample size (21). The Dice score CI was calculated only with Equation (3), while the Pearson correlation coefficient CI used an additional formula for the Fisher z transformation. The Fisher z transformation formula converted the Pearson correlation coefficient, r, into a normal distribution. The Fisher z-transformation formula is:

$$r_z = \frac{1}{2} \ln \frac{1+r}{1-r} \quad (3),$$

where r_z is the Pearson correlation coefficient in the Fisher domain, and r is the Pearson correlation coefficient (22). A CI was calculated in this Fisher domain, and the CI for r was derived by back transforming the limits in the Fisher domain into the r domain using the inverse of the Fisher z transformation defined in Equation (3). The statistical analysis was done with the open-source Python library, Scipy, version 1.4.1.

Results

Data Set Characteristics

The data set for all three U-Nets consisted of 242 T2-weighted images (6292 axial images) in 242 patients. The average age was 64 years (range, 41–96 years). The prostate lesions in the data set had the following PI-RADS score distribution: 5 (36 lesions), 4 (64 lesions), 3 (106 lesions), 2 (45 lesions), and 1 (two lesions). All 242 of the 242 T2-weighted images successfully had bounding boxes created. The 242 T2-weighted images were divided into three data sets: training, validation, and test.

Model Development and Processing Time

U-Net$_A$ trained for approximately 7 hours, while U-Net$_B$ and U-Net$_C$ each trained for 5 hours. While running on a single graphics processing unit, the three U-Nets completed their tasks of bounding box creation, prostate segmentation, and

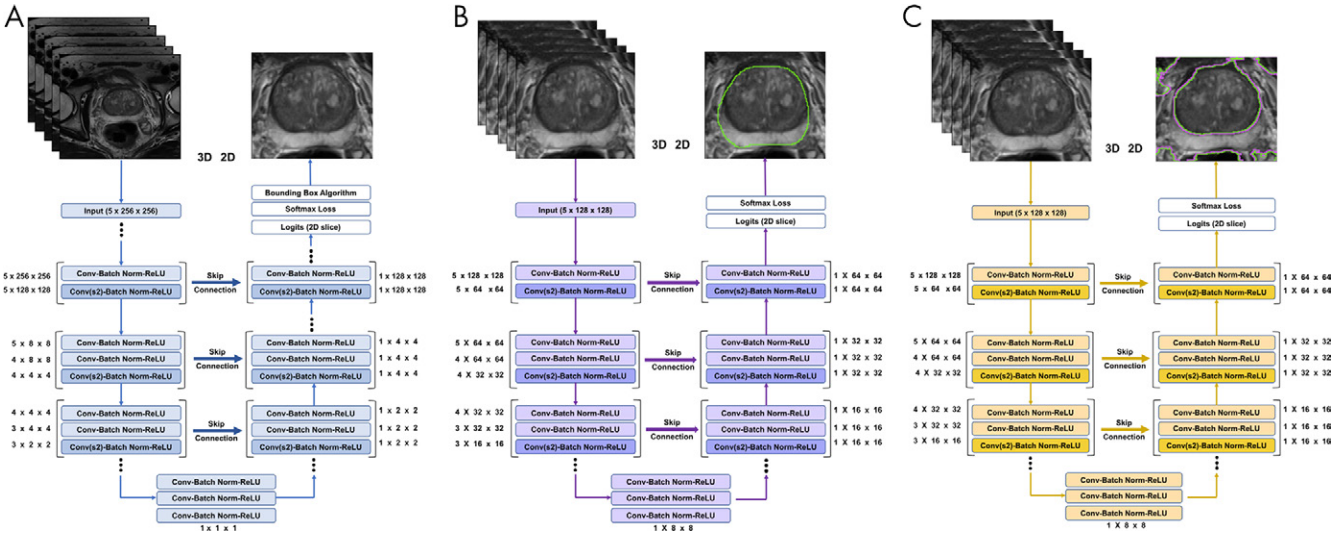

Figure 4: *A*, U-Net$_A$ neural network architecture. U-Net$_A$ localizes the prostate by creating a bounding box around it and narrows the field of view (see Appendix E1 [supplement]). The image is processed with nine layers that consist of convolutions (Convs), batch normalization (Batch Norm), and rectified linear unit (ReLU) activation. Both the contraction and expansion pathways use convolutional kernels that have 1 × 3 × 3 and 2 × 1 × 1 filters. The image is downsampled to a 1 × 1 × 1 matrix before it is upsampled. *B*, U-Net$_B$ neural network architecture. U-Net$_B$ completes prostate organ segmentation by classifying each pixel as either belonging to the prostate or background. The image is processed with six layers that consist of convolutions, batch normalization, and ReLU activation. The contraction and expansion pathways use convolutional kernels that have 1 × 3 × 3 and 2 × 1 × 1 filters. The image is collapsed to a 1 × 8 × 8 image before it is expanded. *C*, U-Net$_C$ neural network architecture. U-Net$_C$ differentiates between transition zone and peripheral zone by classifying every voxel in the image as one of these two classes. This classification then identifies the border between these two prostate regions. U-Net$_C$ has the same architecture as U-Net$_B$ and implements six layers that perform convolutions, batch normalization, and ReLU activation. The convolutional kernels use 1 × 3 × 3 and 2 × 1 × 1 filters. The image is downsampled to a 1 × 8 × 8 image before it is upsampled. 3D = three dimensional, 2D = two dimensional.

prostate zone classification in 0.196 second, 0.226 second, and 0.219 second, respectively.

Segmentation Performance

The output of U-Net$_A$ was supplied to U-Net$_B$ for prostate segmentation, which resulted in an overall median Dice score of 0.952 and a mean Dice score of 0.940 (interquartile range: 0.930–0.961). The prostate Pearson correlation coefficient for volume approximation was 0.981 (95% CI: 0.966, 0.989).

During inference, the prostate segmentations that were made from U-Net$_B$ were then combined with the classifications from U-Net$_C$. By using the outputs from U-Net$_B$ and U-Net$_C$, the final segmentations for TZ and PZ were created. The TZ had an overall median Dice score of 0.920 and a mean Dice score of 0.910 (interquartile range, 0.894–0.938). The TZ Pearson correlation coefficient for volume approximation was 0.992 (95% CI: 0.985, 0.995). The PZ had an overall median Dice score of 0.782 and a mean Dice score of 0.774 (interquartile range, 0.727–0.832). The PZ Pearson correlation coefficient for volume approximation was 0.927 (95% CI: 0.870, 0.957). The accuracy of volume approximation is demonstrated with Bland-Altman plots (Fig 3). All results were calculated with the test data set. Three accessions that illustrate inference performing well are shown in Figure 5. Two accessions that show inference for challenging cases are shown in Figure 6.

Discussion

This study demonstrates that deep learning algorithms are accurate and effective in segmenting the TZ and PZ with mean Dice scores of 0.910 and 0.774, respectively. This study fulfills its goal of showing the feasibility of a machine learning algorithm to segment the prostate and two prostate zones automatically. Differentiation between TZ and PZ is clinically relevant for PI-RADS scoring because the first decision in determining a lesion's score involves assessing its location as either in the TZ or PZ (8). By accomplishing these initial steps in PI-RADS grading of multiparametric MRI, this study supports the subsequent development of a machine learning–based automated PI-RADS scoring algorithm. A software tool that could enhance radiologists' PI-RADS scores is highly desired because PI-RADS scoring and reproducibility is challenging. In a study by Glazer et al (23), PI-RADS score interobserver reproducibility was moderate in the PZ (κ = 0.46) and modest in the TZ (κ = 0.36), where κ represents Cohen kappa coefficient.

As a first step toward PI-RADS automation, prostate segmentation must first be completed. Multiple studies have demonstrated that this task can be accomplished with deep learning at multiparametric MRI and US (24,25). Eight different CNNs with data sets of 40 to 163 patients achieved Dice scores between 0.85 and 0.93 for prostate segmentation (10,13,26–30). A study by Tian et al (26) applied a deep learning algorithm on a data set of 140 patients to achieve a Dice score of 0.85. Similarly, Cheng et al (29) used a deep learning algorithm with an active appearance model to obtain a Dice score of 0.93 with a data set of 120 patients. Many studies have attempted prostate segmentation due to the online data set PROMISE12 that contained prostate MR images with well-curated prostate organ labels (31).

Although substantial progress has been shown in prostate segmentation, TZ and PZ segmentation has been more

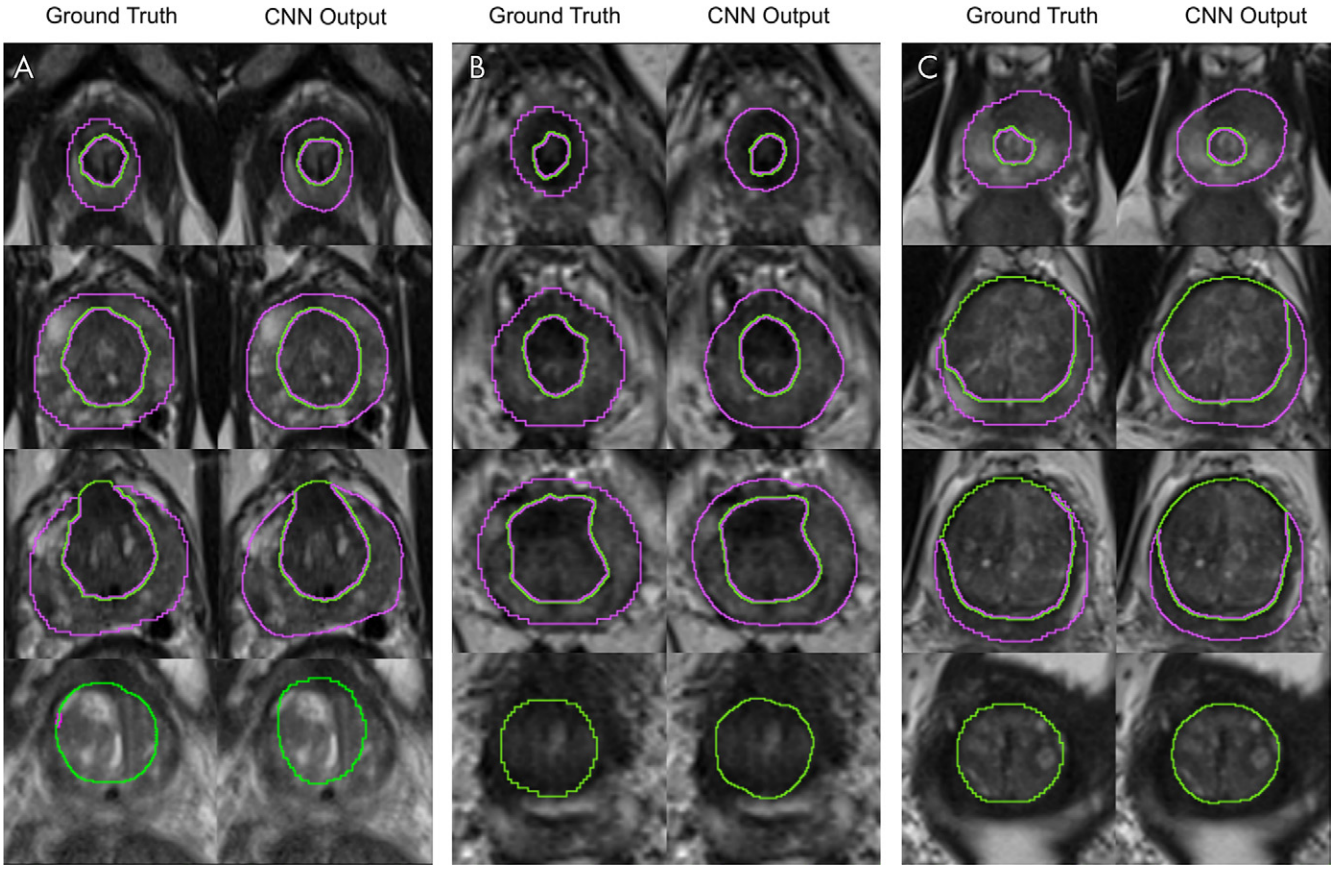

Figure 5: Example segmentations in three patients with *A*, transition zone (TZ) Dice score of 0.940 and a peripheral zone (PZ) Dice score of 0.902, *B*, TZ Dice score of 0.910 and a PZ Dice score of 0.869, and *C*, TZ Dice score of 0.978 and a PZ Dice score of 0.907. CNN = convolutional neural network. Green and pink borders indicate TZ and PZ, respectively.

challenging. Two obstacles include a lack of data and network architectures that do not recognize both TZ and PZ. Although studies by Chilali et al (32) and Makni et al (33) both employed C-means clustering for TZ and PZ segmentation, their results were limited due to their data set sizes of 35 patients and 31 patients, respectively. Similarly, Mooij et al (34), Jensen et al (35), Rundo et al (36), and Zabihooly et al (37) executed U-Nets that yielded results with data sets of 53 patients, 40 patients, 40 patients, and 225 patients, respectively. In addition to small data sets, network architecture has prevented several studies from recognizing the prostate organ, TZ, and PZ. Clark et al (10), Zhu et al (14), and Zavala-Romero et al (38) designed studies that reported only the entire prostate and the PZ with data sets of 134 patients, 163 patients, and 550 patients, respectively. Allen et al (11) and Yin et al (39) implemented algorithms that recognized only the prostate and central gland.

Our work builds upon these previous studies by using larger data set sizes and creating a deep learning algorithm that recognized the prostate organ, TZ, and PZ. Prostate organ, TZ, and PZ segmentations were completed with a data set size of 242 patients. Our network used two U-Nets in parallel that concurrently accomplished different tasks: $U\text{-}Net_B$ was constructed to localize the prostate, while $U\text{-}Net_C$ was implemented to classify every pixel as TZ or PZ. As a result of this architecture, each individual U-Net's hyperparameters could be tuned to optimize its dedicated task. Ultimately, this design allowed us to achieve a rapid and accurate zonal segmentation.

Several limitations should be considered when examining our results. Although our sample size was larger than prior studies, they were limited to our single academic center, and compatibility with different data sets was not tested. Second, our MRI data were obtained from two scanner manufacturers, and further work would be required to evaluate whether this deep learning algorithm could perform well on another manufacturer's hardware as well. Our study was limited by the reliance on a single abdominal radiologist to determine the ground truth. Because the prostate and its zones can be difficult to segment, another radiologist could potentially segment different regions as the ground truth. Future work should include prostate lesion localization and determining whether the lesion belongs in the TZ or PZ. After lesion localization and zone location has been completed, the lesion could be assigned a PI-RADS score. The feasibility of determining PI-RADS score with an isolated lesion was demonstrated in a study by Sanford et al (40).

This study demonstrates that a deep learning architecture composed of U-Nets can accurately and rapidly segment the prostate's TZ and PZ.

Author contributions: Guarantors of integrity of entire study, M.B., R.H., C. Chantaduly, C. Chahine, D.C., P.C.; study concepts/study design or data acquisi-

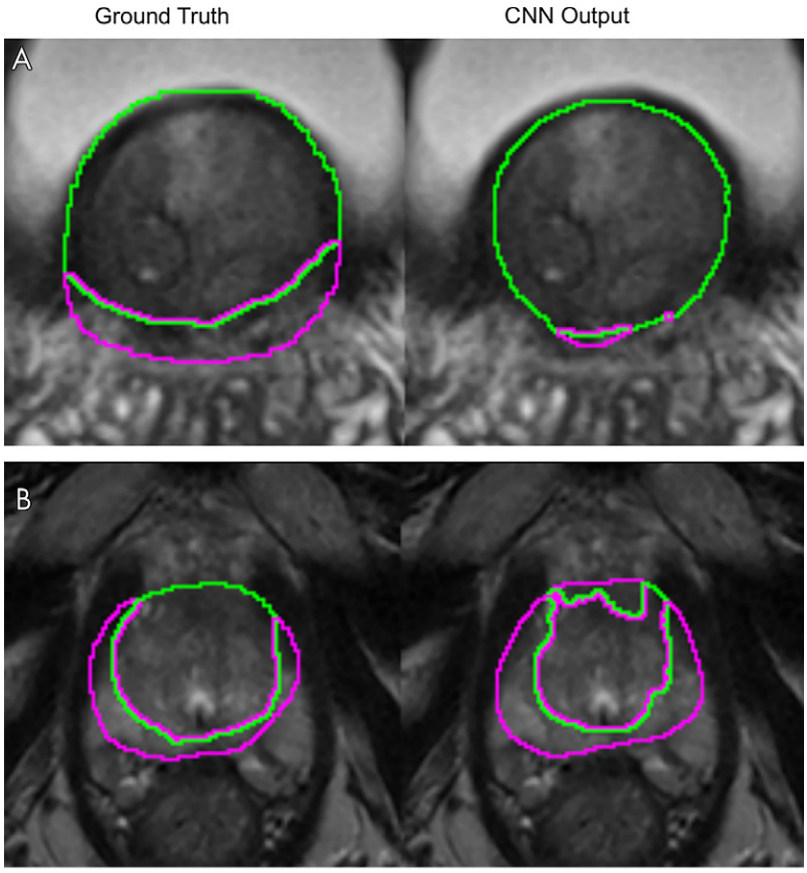

Figure 6: Examples of challenging segmentations. *A,* Segmentation resulted in a peripheral zone (PZ) Dice score of 0.642 and a transition zone (TZ) Dice score of 0.893. *B,* Segmentation resulted in a PZ Dice score of 0.669 and a TZ Dice score of 0.955. Both the TZ and PZ are more challenging for the neural networks to segment at the prostate base. Green and pink borders indicate TZ and PZ, respectively. CNN = convolutional neural network.

tion or data analysis/interpretation, all authors; manuscript drafting or manuscript revision for important intellectual content, all authors; approval of final version of submitted manuscript, all authors; agrees to ensure any questions related to the work are appropriately resolved, all authors; literature research, M.B., R.H., A.U., C. Chahine, D.C., P.C.; clinical studies, R.H., C. Chantaduly, A.U., D.C., P.C.; statistical analysis, M.B., C. Chantaduly, C. Chahine, P.C.; and manuscript editing, all authors

Disclosures of Conflicts of Interest: M.B. Activities related to the present article: disclosed no relevant relationships. Activities not related to the present article: author is a recipient of Radiological Society of North America Medical Student Research Grant (RMS1902) and recipient of Alpha Omega Alpha Carolyn L. Kuckein Student Research Fellowship. Other relationships: disclosed no relevant relationships. **R.H.** disclosed no relevant relationships. **C. Chantaduly** disclosed no relevant relationships. **K.T.H.** disclosed no relevant relationships. **A.U.** disclosed no relevant relationships. **C. Chahine** disclosed no relevant relationships. **M.R.** disclosed no relevant relationships. **D.C.** Activities related to the present article: disclosed no relevant relationships. Activities not related to the present article: author received consultancy fees from Canon Medical; author is employed by University of California, Irvine; author received money from Cullins and Grandy for expert testimony; author has stock/stock options in Avicenna.ai. Other relationships: disclosed no relevant relationships. **P.C.** Activities related to the present article: disclosed no relevant relationships. Activities not related to the present article: author received payment for lectures including service on speakers bureaus from Canon Medical; author is a cofounder of and has stock/stock options in Avicenna.ai. Other relationships: disclosed no relevant relationships.

References

1. Siegel RL, Miller KD, Jemal A. Cancer statistics, 2016. CA Cancer J Clin 2016;66(1):7–30.
2. Bray F, Ferlay J, Soerjomataram I, Siegel RL, Torre LA, Jemal A. Global cancer statistics 2018: GLOBOCAN estimates of incidence and mortality worldwide for 36 cancers in 185 countries. CA Cancer J Clin 2018;68(6):394–424 [Published correction appears in CA Cancer J Clin 2020;70(4):313.].
3. Schröder FH, Hugosson J, Roobol MJ, et al. Screening and prostate-cancer mortality in a randomized European study. N Engl J Med 2009;360(13):1320–1328.
4. Hugosson J, Carlsson S. Overdetection in screening for prostate cancer. Curr Opin Urol 2014;24(3):256–263.
5. Bangma CH, Roemeling S, Schröder FH. Overdiagnosis and overtreatment of early detected prostate cancer. World J Urol 2007;25(1):3–9.
6. Thompson IM, Pauler DK, Goodman PJ, et al. Prevalence of prostate cancer among men with a prostate-specific antigen level < or =4.0 ng per milliliter. N Engl J Med 2004;350(22):2239–2246.
7. Nguyentat M, Ushinsky A, Miranda-Aguirre A, et al. Validation of Prostate Imaging-Reporting and Data System Version 2: A Retrospective Analysis. Curr Probl Diagn Radiol 2018;47(6):404–409.
8. Purysko AS, Rosenkrantz AB, Barentsz JO, Weinreb JC, Macura KJ. PI-RADS Version 2: A Pictorial Update. RadioGraphics 2016;36(5):1354–1372.
9. Padhani AR, Weinreb J, Rosenkrantz AB, Villeirs G, Turkbey B, Barentsz J. Prostate Imaging-Reporting and Data System Steering Committee: PI-RADS v2 Status Update and Future Directions. Eur Urol 2019;75(3):385–396.
10. Clark T, Zhang J, Baig S, Wong A, Haider MA, Khalvati F. Fully automated segmentation of prostate whole gland and transition zone in diffusion-weighted MRI using convolutional neural networks. J Med Imaging (Bellingham) 2017;4(4):041307.
11. Allen PD, Graham J, Williamson DC, Hutchinson CE. Differential segmentation of the prostate in MR images using combined 3D shape modelling and voxel classification. In: 3rd IEEE International Symposium on Biomedical Imaging: Nano to Macro, 2006, Arlington, VA, April 6–9, 2006. Piscataway, NJ: IEEE, 2006; 410–413.

12. Shaver MM, Kohanteb PA, Chiou C, et al. Optimizing Neuro-Oncology Imaging: A Review of Deep Learning Approaches for Glioma Imaging. Cancers (Basel) 2019;11(6):829.
13. Zhu Q, Du B, Turkbey B, Choyke PL, Yan P. Deeply-supervised CNN for prostate segmentation. In: 2017 International Joint Conference on Neural Networks (IJCNN), Anchorage, AK, May 14–19, 2017. Piscataway, NJ: IEEE, 2017; 178–184.
14. Zhu Y, Wei R, Gao G, et al. Fully automatic segmentation on prostate MR images based on cascaded fully convolution network. J Magn Reson Imaging 2019;49(4):1149–1156.
15. Bardis M, Houshyar R, Chantaduly C, et al. Deep Learning with Limited Data: Organ Segmentation Performance by U-Net. Electronics (Basel) 2020;9(8):1199.
16. Ushinsky A, Bardis M, Glavis-Bloom J, et al. A 3D-2D Hybrid U-Net Convolutional Neural Network Approach to Prostate Organ Segmentation of Multiparametric MRI. AJR Am J Roentgenol 2021;216(1):111–116.
17. Ronneberger O, Fischer P, Brox T. U-Net: Convolutional Networks for Biomedical Image Segmentation. In: Navab N, Hornegger J, Wells W, Frangi A, eds. Medical Image Computing and Computer-Assisted Intervention – MICCAI 2015. MICCAI 2015. Lecture Notes in Computer Science, vol 9351. Cham, Switzerland: Springer, 2015; 234–241.
18. He K, Zhang X, Ren S, Sun J. Deep Residual Learning for Image Recognition. In: 2016 IEEE Conference on Computer Vision and Pattern Recognition (CVPR), Las Vegas, NV, June 27–30, 2016. Piscataway, NJ: IEEE, 2016; 770–778.
19. Kingma DP, Ba J. Adam: A method for stochastic optimization. arXiv arXiv:1412.6980 [preprint] https://arxiv.org/abs/1412.6980. Posted December 22, 2014. Accessed February 1, 2020.
20. Zou KH, Warfield SK, Bharatha A, et al. Statistical validation of image segmentation quality based on a spatial overlap index. Acad Radiol 2004;11(2):178–189.
21. Hazra A. Using the confidence interval confidently. J Thorac Dis 2017;9(10):4125–4130.
22. Asuero AG, Sayago A, Gonzalez A. The correlation coefficient: An overview. Crit Rev Anal Chem 2006;36(1):41–59.
23. Glazer DI, Mayo-Smith WW, Sainani NI, et al. Interreader Agreement of Prostate Imaging Reporting and Data System Version 2 Using an In-Bore MRI-Guided Prostate Biopsy Cohort: A Single Institution's Initial Experience. AJR Am J Roentgenol 2017;209(3):W145–W151.
24. van Sloun RJG, Wildeboer RR, Mannaerts CK, et al. Deep learning for real-time, automatic, and scanner-adapted prostate (zone) segmentation of transrectal ultrasound, for example, magnetic resonance imaging–transrectal ultrasound fusion prostate biopsy. Eur Urol Focus 2019. 10.1016/j.euf.2019.04.009. Published online April 23, 2019.
25. Bardis MD, Houshyar R, Chang PD, et al. Applications of Artificial Intelligence to Prostate Multiparametric MRI (mpMRI): Current and Emerging Trends. Cancers (Basel) 2020;12(5):1204.
26. Tian Z, Liu L, Zhang Z, Fei B. PSNet: prostate segmentation on MRI based on a convolutional neural network. J Med Imaging (Bellingham) 2018;5(2):021208.
27. Karimi D, Samei G, Kesch C, Nir G, Salcudean SE. Prostate segmentation in MRI using a convolutional neural network architecture and training strategy based on statistical shape models. Int J CARS 2018;13(8):1211–1219.
28. Milletari F, Navab N, Ahmadi SA. V-Net: Fully Convolutional Neural Networks for Volumetric Medical Image Segmentation. In: 2016 Fourth International Conference on 3D Vision (3DV), Stanford, CA, October 25–28, 2016. Piscataway, NJ: IEEE, 2016; 565–571.
29. Cheng R, Roth HR, Lu L, et al. Active appearance model and deep learning for more accurate prostate segmentation on MRI. In: Styner MA, Angelini ED, eds. Proceedings of SPIE: medical imaging 2016—image processing. Vol 9784. Bellingham, Wash: International Society for Optics and Photonics, 2016; 97842I.
30. Wang B, Lei Y, Tian S, et al. Deeply supervised 3D fully convolutional networks with group dilated convolution for automatic MRI prostate segmentation. Med Phys 2019;46(4):1707–1718.
31. Litjens G, Toth R, van de Ven W, et al. Evaluation of prostate segmentation algorithms for MRI: the PROMISE12 challenge. Med Image Anal 2014;18(2):359–373.
32. Chilali O, Puech P, Lakroum S, Diaf M, Mordon S, Betrouni N. Gland and zonal segmentation of prostate on T2W MR images. J Digit Imaging 2016;29(6):730–736.
33. Makni N, Iancu A, Colot O, Puech P, Mordon S, Betrouni N. Zonal segmentation of prostate using multispectral magnetic resonance images. Med Phys 2011;38(11):6093–6105.
34. Mooij G, Bagulho I, Huisman H. Automatic segmentation of prostate zones. arXiv:1806.07146 [preprint] https://arxiv.org/abs/1806.07146. Posted June 19, 2018. Accessed February 1, 2020.
35. Jensen C, Sørensen KS, Jørgensen CK, et al. Prostate zonal segmentation in 1.5T and 3T T2W MRI using a convolutional neural network. J Med Imaging (Bellingham) 2019;6(1):014501.
36. Rundo L, Han C, Zhang J, et al. CNN-based Prostate Zonal Segmentation on T2-weighted MR Images: A Cross-dataset Study. arXiv:1903.12571 [preprint] https://arxiv.org/abs/1903.12571. Posted March 29, 2019. Accessed February 1, 2020.
37. Zabihollahy F, Schieda N, Krishna Jeyaraj S, Ukwatta E. Automated segmentation of prostate zonal anatomy on T2-weighted (T2W) and apparent diffusion coefficient (ADC) map MR images using U-Nets. Med Phys 2019;46(7):3078–3090.
38. Zavala-Romero O, Breto AL, Xu IR, et al. Segmentation of prostate and prostate zones using deep learning : A multi-MRI vendor analysis. Strahlenther Onkol 2020;196(10):932–942.
39. Yin Y, Fotin SV, Periaswamy S, et al. Fully automated 3D prostate central gland segmentation in MR images: a LOGISMOS based approach. In: Haynor DR, Ourselin S, eds. Proceedings of SPIE: medical imaging 2012—image processing. Vol 8314. Bellingham, Wash: International Society for Optics and Photonics, 2012; 83143B.
40. Sanford T, Harmon SA, Turkbey EB, et al. Deep-Learning-Based Artificial Intelligence for PI-RADS Classification to Assist Multiparametric Prostate MRI Interpretation: A Development Study. J Magn Reson Imaging 2020;52(5):1499–1507.